AFRL-AFOSR-VA-TR-2016-0098

Flapping and Rotary Wing Lift at Low Reynolds Number

Anya Jones
MARYLAND UNIV COLLEGE PARK

02/26/2016
Final Report

Air Force Research Laboratory
AF Office Of Scientific Research (AFOSR)/ RTB1
Arlington, Virginia 22203
Air Force Materiel Command

REPORT DOCUMENTATION PAGE

Form Approved
OMB No. 0704-0188

1. REPORT DATE *(DD-MM-YYYY)* 12-02-2016	**2. REPORT TYPE** Final Report	**3. DATES COVERED** *(From - To)* 15-05-2012 to 14-11-2015

4. TITLE AND SUBTITLE
Lift Production on Flapping and Rotary Wings at Low Reynolds Numbers (YIP)

5a. CONTRACT NUMBER

5b. GRANT NUMBER
FA9550-12-1-0251

5c. PROGRAM ELEMENT NUMBER

6. AUTHOR(S)
Jones, Anya

5d. PROJECT NUMBER

5e. TASK NUMBER

[Type a quote from the document or the summary of an interesting point. You can position the text box anywhere in the document. Use the Drawing Tools tab to change the formatting of the pull quote text box.]

7. PERFORMING ORGANIZATION NAME(S) AND ADDRESS(ES)
University of Maryland, College Park

9. SPONSORING/MONITORING AGENCY NAME(S) AND ADDRESS(ES)
Air Force Office of Scientific Research
875 N. Randolph Street
Arlington, VA 22203

10. SPONSOR/MONITOR'S ACRONYM(S)
AFOSR

11. SPONSOR/MONITOR'S REPORT NUMBER(S)

12. DISTRIBUTION/AVAILABILITY STATEMENT
DISTRIBUTION A

13. SUPPLEMENTARY NOTES

14. ABSTRACT

The objective of this research was to identify the mechanisms of lift production on models of an entomological flapping wing stroke by evaluating the relative importance of the leading edge vortex, other coherent vortical structures in the flow, bound circulation, and non-circulatory forcing. The entomological wing stroke was modeled as a combination of wing pitch and rotation. In collaboration with the NATO AVT-202 task group on ``Extensions of Fundamental Flow Physics to Practical MAV Aerodynamics", the rectilinear analogs of these rotational motions were also studied.By comparing both pitching and surging wings in rectilinear and rotational motion over a range of accelerations, it was found that the strength and trajectory of the leading edge vortex had a significant impact on the lift production of a wing undergoing highly unsteady kinematics. The vortex need not be attached to the wing to affect a lift force.

15. SUBJECT TERMS
leading edge vortex, flapping wing, unsteady lift, rotating wing

16. SECURITY CLASSIFICATION OF:			**17. LIMITATION OF ABSTRACT**	**18. NUMBER OF PAGES**	**19a. NAME OF RESPONSIBLE PERSON**
a. REPORT	**b. ABSTRACT**	**c. THIS PAGE**			**19b. TELEPHONE NUMBER** *(Include area code)*

Reset

INSTRUCTIONS FOR COMPLETING SF 298

1. REPORT DATE. Full publication date, including day, month, if available. Must cite at least the year and be Year 2000 compliant, e.g. 30-06-1998; xx-06-1998; xx-xx-1998.

2. REPORT TYPE. State the type of report, such as final, technical, interim, memorandum, master's thesis, progress, quarterly, research, special, group study, etc.

3. DATES COVERED. Indicate the time during which the work was performed and the report was written, e.g., Jun 1997 - Jun 1998; 1-10 Jun 1996; May - Nov 1998; Nov 1998.

4. TITLE. Enter title and subtitle with volume number and part number, if applicable. On classified documents, enter the title classification in parentheses.

5a. CONTRACT NUMBER. Enter all contract numbers as they appear in the report, e.g. F33615-86-C-5169.

5b. GRANT NUMBER. Enter all grant numbers as they appear in the report, e.g. AFOSR-82-1234.

5c. PROGRAM ELEMENT NUMBER. Enter all program element numbers as they appear in the report, e.g. 61101A.

5d. PROJECT NUMBER. Enter all project numbers as they appear in the report, e.g. 1F665702D1257; ILIR.

5e. TASK NUMBER. Enter all task numbers as they appear in the report, e.g. 05; RF0330201; T4112.

5f. WORK UNIT NUMBER. Enter all work unit numbers as they appear in the report, e.g. 001; AFAPL30480105.

6. AUTHOR(S). Enter name(s) of person(s) responsible for writing the report, performing the research, or credited with the content of the report. The form of entry is the last name, first name, middle initial, and additional qualifiers separated by commas, e.g. Smith, Richard, J, Jr.

7. PERFORMING ORGANIZATION NAME(S) AND ADDRESS(ES). Self-explanatory.

8. PERFORMING ORGANIZATION REPORT NUMBER. Enter all unique alphanumeric report numbers assigned by the performing organization, e.g. BRL-1234; AFWL-TR-85-4017-Vol-21-PT-2.

9. SPONSORING/MONITORING AGENCY NAME(S) AND ADDRESS(ES). Enter the name and address of the organization(s) financially responsible for and monitoring the work.

10. SPONSOR/MONITOR'S ACRONYM(S). Enter, if available, e.g. BRL, ARDEC, NADC.

11. SPONSOR/MONITOR'S REPORT NUMBER(S). Enter report number as assigned by the sponsoring/ monitoring agency, if available, e.g. BRL-TR-829; -215.

12. DISTRIBUTION/AVAILABILITY STATEMENT. Use agency-mandated availability statements to indicate the public availability or distribution limitations of the report. If additional limitations/ restrictions or special markings are indicated, follow agency authorization procedures, e.g. RD/FRD, PROPIN, ITAR, etc. Include copyright information.

13. SUPPLEMENTARY NOTES. Enter information not included elsewhere such as: prepared in cooperation with; translation of; report supersedes; old edition number, etc.

14. ABSTRACT. A brief (approximately 200 words) factual summary of the most significant information.

15. SUBJECT TERMS. Key words or phrases identifying major concepts in the report.

16. SECURITY CLASSIFICATION. Enter security classification in accordance with security classification regulations, e.g. U, C, S, etc. If this form contains classified information, stamp classification level on the top and bottom of this page.

17. LIMITATION OF ABSTRACT. This block must be completed to assign a distribution limitation to the abstract. Enter UU (Unclassified Unlimited) or SAR (Same as Report). An entry in this block is necessary if the abstract is to be limited.

Lift Production on Flapping and Rotary Wings at Low Reynolds Numbers (YIP)

FA9550-12-1-0251

Final Report, February 2016

PI: Dr. Anya R. Jones
Department of Aerospace Engineering, University of Maryland, College Park

1 Abstract

The objective of this research was to identify the mechanisms of lift production on models of an entomological flapping wing stroke by evaluating the relative importance of the leading edge vortex, other coherent vortical structures in the flow, bound circulation, and non-circulatory forcing. The entomological wing stroke was modeled as a combination of wing pitch and rotation. In collaboration with the NATO AVT-202 task group on "Extensions of Fundamental Flow Physics to Practical MAV Aerodynamics", the rectilinear analogs of these rotational motions were also studied. To identify lift-generating mechanisms and relate flow structures to the unsteady forces generated by the wing, synchronized flow visualization, force measurements, and particle image velocimetry (PIV) were recorded for a variety of wing kinematics over a large parameter space. It was found that although the three-dimensionality of the rotational motions resulted in an attached leading edge vortex whereas the leading edge vortex was shed from a wing in rectilinear translation. Wing loading on the rotating wing was such that the resulting lift coefficients were, however, similar. The introduction of an unsteady pitching moment had a greater impact on the lift transient. By comparing both pitching and surging wings in rectilinear and rotational motion over a range of accelerations, it was found that the strength and trajectory of the leading edge vortex had a significant impact on the lift production of a wing undergoing highly unsteady kinematics. The vortex need not be attached to the wing to affect a lift force, and trends in vortex characteristics were found when scaled by the velocity normal to the leading edge of the wing.

2 Introduction

Early rotating wing experiments identified an attached leading edge vortex that produced high lift, particularly in the early stages of the wing stroke, between 60 and 120 degrees of revolution (after the initial startup transient, but before the quasi-steady state developed) [3, 6, 15, 28]. Later experiments focused on the first 90 degrees of rotation and found that lift values are very high in the first chord-length (approximately 12 degrees) of motion while the initial vortex forms and before it detaches from the wing and is swept downstream [10]. Although kinematics, angle of attack, and aspect ratio were not found to have a significant effect on the flow structure, the timing of the leading edge vortex formation was found to be affected by Reynolds number [11].

Many previous experiments have focused on the formation and shedding of the leading edge vortex with little or no attention to the tip vortex. Some experiments on rotating wings at Reynolds numbers between 1,000 and 5,000 have revealed a three-dimensional vortex loop that connects the leading edge vortex, the tip vortex, and the trailing edge (or starting) vortex [5, 13]. It is thought that the loop structure stabilizes the leading edge vortex by allowing vorticity generated at the leading edge to drain from the LEV into the tip vortex. At higher Reynolds numbers (Re = 8,000), periodically shedding vortices have been observed on a mechanical wing flapper [27]. At Reynolds numbers between 10,000 and 60,000 little interaction between the leading edge and tip vortices has been observed and LEVs repeatedly form and shed on a rotating wing [11]. Even very near the wing tip, the LEVs that formed were highly two-dimensional and variations in aspect ratio, angle of attack, and Reynolds number were found to have an insignificant effect on the structure of the flow and the time-history of lift [10, 11].

The objective of this research was to identify the mechanisms of lift production on models of an entomological flapping wing stroke by evaluating the relative importance of the leading edge vortex (LEV), other coherent vortical structures in the flow (e.g. tip and trailing edge vortices), bound circulation, and non-circulatory forcing. The entomological wing stroke was modeled as a combination of wing pitch and rotation. These canonical wing kinematics produced well-characterized wing strokes that preserved the spanwise velocity gradient that exists during the translational phases of a natural wing stroke, the wing starting/stopping accelerations, and the large changes in pitch that are experienced during the rotational phases of a natural wing stroke. In collaboration with the NATO AVT-202 task group on "Extensions of Fundamental Flow Physics to Practical MAV Aerodynamics", the rectilinear analogs of these rotational motions were also studied. The goal of this research is to determine what conditions affect the relative importance of these phenomena to lift production over the time scale of a single wing stroke.

3 Methodology

3.1 Wing Kinematics

The NATO AVT-202 task group "Extensions of Fundamental Flow Physics to Practical MAV Aerodynamics" defined four canonical test cases [1], illustrated in Figure 1. Cases 1A and 1B are two-dimensional rectilinear motions in which the relative flow is constant along the finite span of the wing. For these cases, the wing was towed along the length of a towing tank at either a fixed angle of attack (rectilinear surge), or towed at constant speed while being pitched from zero to non-zero (rectilinear pitch). Cases 2A and 2B are the rotational versions of these motions and the focus of the current work. The rotational kinematics are three-dimensional in that the relative flow varies along the wing span. In these cases, the wing was rotated about an axis near its root in a propeller-like motion. Again, the wing is either at a fixed incidence (rotational surge) or pitched to some angle of attack α during a constant-speed surge (rotational pitch). Each of the four cases is further defined such that there exists a "fast" and "slow" version over which the unsteady motion of the wing (in either pitch or surge) occurs over 1 or 6 chord-lengths of travel, respectively. In the rotational cases, this distance was defined by the arc length s at 75% of the tip radius. It should be noted that even the "slow" case as defined here is a highly unsteady motion with a reduced time well above that considered quasi-steady. The wing kinematics are shown schematically in Figure 2(a). The velocity profile is defined by a linear ramp in either pitch (α) or surge (U) to the final state, with some degree of smoothing applied at the sharp corners of this profile. In the pitch case, the wing starts rotation at zero incidence and pitches to $\alpha = 45^\circ$. In the surge case, the wing is started from rest at 45° incidence and is driven in pure rotation. The baseline Reynolds number was 20,000 (defined at 75% of the tip radius for the rotational cases), though parameter variations were also performed. For the rotating cases, the wing was an aspect ratio 2 rectangular flat plate, and the root cutout (i.e., the distance from the axis of rotation to the wing root) is $0.5c$ as shown in Figure 2(b). For the rectilinear cases, the wing was an aspect ratio 4 rectangular flat plate.

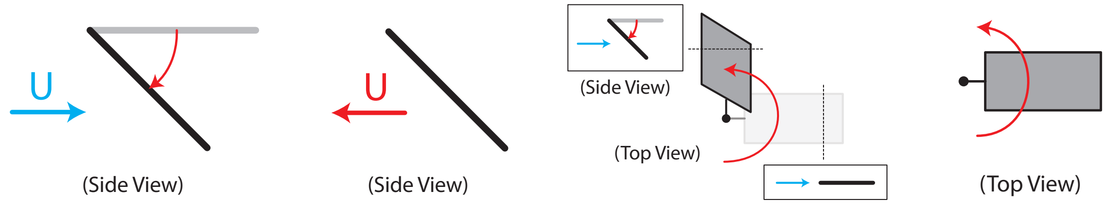

(a) 1A: Rectilinear pitch (b) 1B: Rectilinear surge (c) 2A: Rotational pitch (d) 2B: Rotational surge

Figure 1: AVT-202 canonical test cases, adapted from Ref. 1.

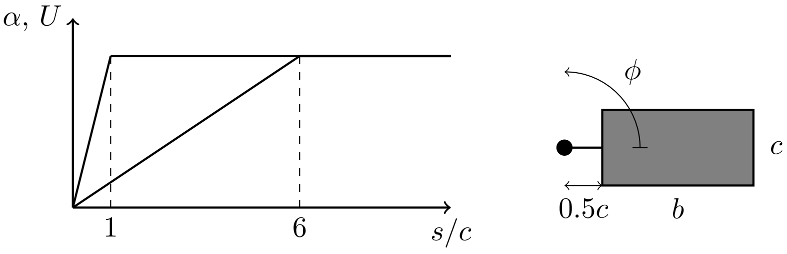

(a) Rotational wing kinematics (b) Æ=2 flat plate wing

Figure 2: Schematic of the AVT-202 rotating wing kinematics and geometry, from Ref. 12.

3.2 Experimental Setup

Rotating wing experiments were performed at the University of Maryland in a 1.25m×1.25m×1.25m tank of quiescent water (early experiments in surge only) and a 7m × 1.5m × 1m towing tank (extensive experiments in both surge and pitch). The towing tank is equipped with a 4-axis motion control system for computer-controlled model motion. The motor assembly, shown in Figure 3(a), is mounted on the towing carriage and contains two brushless linear motors, and a direct-drive brushless rotary stage. Vertical plunge (±49 cm) and pitch (±90 deg) are driven by two linear motors and a custom-designed Hoeken linkage. Continuous rotation is provided by the rotary stage. Carriage translation (7 m) is directly driven by a pair of brushless linear motors, enabling additional experiments on the rectilinear motions. All of the stages are equipped with magnetic encoders, and the entire traverse system is controlled using a multi-axis Galil motion controller. Model motion can be controlled to within 0.1 mm; pitch motion is accurate to within 0.1 degrees.

3.3 Measurement Techniques

Direct unsteady **force measurements** were acquired via a submergible ATI Mini40 6-axis force/torque transducer. The transducer has a force resolution of 0.01 N and a torque resolution of 0.0001 N·m. The sampling rate was 1000 Hz. Each case was run 5 times, starting from different locations in the tank, and the results were ensemble-averaged after smoothing the acquired force signal. To isolate only the hydrodynamic loads, contributions from gravity and buoyancy were removed from the measured force. In the surge cases, the average force during the two seconds before the wing motion was taken as the net gravity and buoyancy force, and subtracted from the measurement. Inertial loads were measured in air and were found to be negligible for all of the wing kinematics tested. The force signals acquired were smoothed in time with Matlab's `smooth` function with the `lowess` option set to attenuate the effects of electrical noise and rig vibration, as detailed in Ref. 18.

Planar **particle image velocimetry (PIV)** was performed in the 1.25m × 1.25m × 1.25m

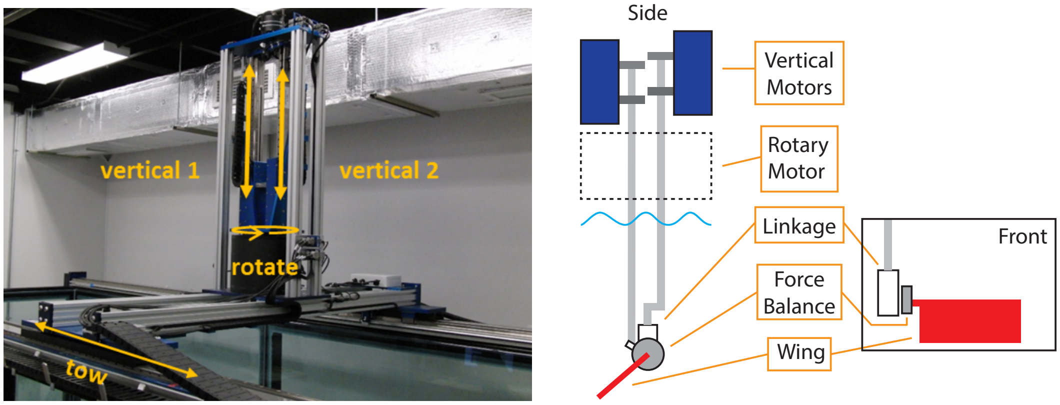

(a) The 4 motion axes and gantry.

(b) Drawing of wing mounting setup.

Figure 3: The University of Maryland tow tank setup, from Ref. 18.

water tank at the University of Maryland. The Reynolds number, defined at 75% of the physical wing span, or 2.15 chords from the axis of rotation, was 25,000. PIV flow fields were measured on chordwise planes at wing span locations of 20, 30, 50, 70, and 80% of the physical wing span, and at azimuthal stroke angles of 10°, 20°, 30°, 60°, 90°, and 180°. The PIV was performed using a double-pulsed Nd:YLF laser (Litron LDY304, 30 mJ/pulse, 10 kHz max). Silver-coated glass spheres with an average diameter of 14 μm were used as the tracer particles. Images were acquired using a Phantom v311 camera (1 MP CMOS sensor, up to 3.2 kHz at max resolution) placed orthogonal to the laser sheet (and orthogonal to the tank wall). After background subtraction (to increase the signal-to-noise ratio), correlation was performed in DaVis v8.1 using square multi-pass interrogation windows and a median filter. Further details of the PIV setup can be found in Refs. [17, 21]. Additional PIV was performed on the rectilinear pitching and surging cases in the 7m × 1.5m × 1m towing tank and in the free-surface water tunnel at AFRL (WPAFB) [19, 20].

3.4 Analysis Techniques

Force and moment measurements were obtained directly from the force balance. The smoothed force signals were normalized such that $C_L = L/(0.5\rho U_f^2 A)$ (where U_f is the steady-state wing velocity and A is the wing area), and are reported here as lift coefficient histories. For the rotational cases, U_f was taken to be the local velocity at 75% of the wing tip radius (or 1.875 chords from the axis of rotation). To further understand the physical sources of lift during the unsteady portions of the wing stroke, force measurements were broken down into two components: circulatory and non-circulatory. When a body accelerates through a fluid, it experiences a non-circulatory inertial force often referred to as “added-mass”. Pitt Ford and Babinsky [24] provide a complex potential analysis for an accelerating rigid flat plate in pure translation and derives the lift coefficient contribution from added-mass as

$$C_L = \frac{\pi}{4}\frac{\left(\frac{dU}{dt}c\right)}{U^2}\sin(2\alpha) \tag{1}$$

where α is the plate's angle of incidence and U is the plate's instantaneous velocity. In the current work, acceleration is constant and the equations becomes

$$C_L = \frac{\pi c}{8a}\sin(2\alpha) \tag{2}$$

where a is the number of chord-lengths traveled during acceleration. From Equation 2, it is evident that the effect of added mass increases with angle of attack. When the wing ceases acceleration, however, the added-mass term goes to zero. The remaining “circulatory” lift may consist of contributions from both bound circulation and leading edge vortices.

The time-resolved velocity fields obtained via PIV were used to compute the vorticity field, as well as to identify and quantify vortical structures in the flow, i.e., the leading edge vortex. The location of the LEV was taken to be the centroid of the Γ_1 function of Graftieaux, et al. [8]. The Γ_1 function, given in Equation (3), characterizes the extent to which the fluid motion is circular around a point.

$$\Gamma_1(P) = \frac{1}{S}\int_S \sin(\theta)\mathrm{d}S \tag{3}$$

Here, S is the area of integration, and θ is the angle between the point P and the velocity vector at $\mathrm{d}S$. The value of the integrand at each point in a vector field is the sine of the angle between the vector from a point of interest to a nearby velocity vector and the relative direction of that velocity. A sine (and thus Γ_1) value of 1 everywhere near P indicates the velocity is purely tangential and the flow is highly rotational about the point of interest. Computing the Γ_1 values for the entire velocity field produces a scalar field with values ranging from -1 to +1, where the sign indicates the direction of rotation. In practice, a threshold is applied so that only areas of strong circular flow are identified; here the Γ_1 field was thresholded at $|\Gamma_1| \geq 0.6$. The centroid of the first such region leaving the leading of the wing and satisfying this threshold was computed and this point was taken as the location of the LEV. The strength of the LEV was taken to be the sum of the lift-promoting vorticity above the wing. This definition includes the feeding shear layer, but excludes the secondary vorticity that is produced on the surface of the plate.

4 Results and Discussion

4.1 Rectilinear Surge

To better understand the more complex three-dimensional rotational cases, experiments and analysis was also performed on the AVT-202 rectilinear cases. These results allowed for comparison to a wide body of literature and provided an opportunity for international collaboration.

4.1.1 Effect of Wing Acceleration on Forcing

A wide range of wing accelerations were tested in both the AFRL water tunnel and the UMD towing tank. Figure 4(a) shows the time-history of the lift coefficient for a wing at $\alpha = 45°$ accelerating over a range of chord-lengths traveled, $s_a/c = \{0.125, 0.25, 0.5, 1, 2, 3, 4, 5, 6\}$. The measured C_L increases with wing acceleration as expected due to non-circulatory effects. Figure 4(b) suggests a rescaling of the x-axis of Figure 4(a) by each respective acceleration distance, s_a/c. Applying the new scaling, each acceleration phase occurs within $0 \leq s/s_a \leq 1$. Additionally, the added mass term from Equation 2 is subtracted from the measured lift to isolate the circulatory force component. Figure 4(b) shows that the circulatory lift curves collapse when $s/s_a \leq 0.4$, indicating a region where circulation growth is independent of acceleration profile. After this region, the curves diverge slightly and peak at $s/s_a = 1$. This result suggests that a main factor corresponding to the difference in lift production between the cases (at least during the acceleration phase) is an increased circulatory force component.

Once the wing motion becomes steady, the added mass contribution goes to zero, leaving only circulatory forces responsible for lift production. Following the peak at the end of acceleration, all

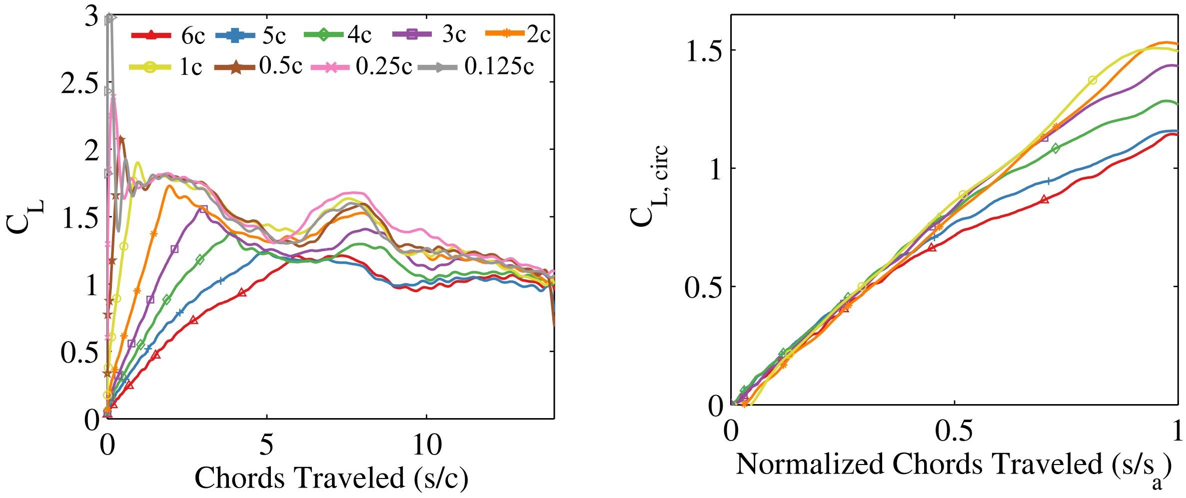

(a)

(b)

Figure 4: Acceleration study at $\alpha = 45°$ for $0.125 \leq s_a/c \leq 6$. (a) Lift coefficient histories. (b) Circulatory component of lift history during each acceleration phase. Convective time, s/c, is scaled by acceleration distance, s_a/c. From Ref. 19.

curves show a decrease in lift, reaching a minimum around $s/c = 5.5 - 6$, except for the $s_a/c = 5$ and 6 cases, which reach minimums around $s/c = 9.5 - 10$. For $s_a/c \leq 4$, the lift once again increases to a second local maximum around $s/c = 7.5 - 8$. After the second lift peak (which arises as a result of vortex formation and shedding [19]), all of the cases tested here gradually decrease in lift until the end of the motion.

Looking more closely at two cases, the "fast case" ($s_a/c = 1$) and a "slow case" ($s_a/c = 6$), consider the force contributions from circulatory and non-circulatory effects during the acceleration of the wing. To isolate the effect of the circulatory forces on lift in the acceleration region, the non-circulatory added-mass force from Equation 2 was removed from the measured force data, as shown in Figure 5. Even after removing the theoretical added-mass force from the two lift curves, there is still a $\Delta\mathrm{C_L}$ between the the cases, (e.g. at $s/c = 1$, $C_{L_{s_a/c=1}} = 1.6$ and $C_{L_{s_a/c=6}} = 0.3$) suggesting that the difference in lift during the transient phase of each acceleration profile is not entirely due to inertial forces, but that circulatory forces provide a significant portion of the measured lift, even during wing acceleration. In both of these cases, wing acceleration is high enough that the added mass force contribution is large, but the circulatory forces quickly overtake the added mass force.

4.1.2 Tracking the Leading Edge Vortex

Figure 6 plots the trajectory of the leading edge vortex in the lab-fixed and wing-fixed frames for the fast and slow cases and shows that both result in nearly identical vortex trajectories with respect to convective time. The leading edge vortex forms immediately upon startup and translates linearly over the first chord of travel. At $s/c \approx 1.25$, both LEVs take an immediate departure from the wing surface, illustrated by Figure 6(c), remaining at a relatively constant X' location (Figure 6(b)).

Vortex trajectory provides the instantaneous position of the vortex, but it does not contain information about its size or strength. Figure 7 shows the leading edge vortex in the form of vorticity plots, demonstrating a clear difference between the two cases. The fast surge case forms a

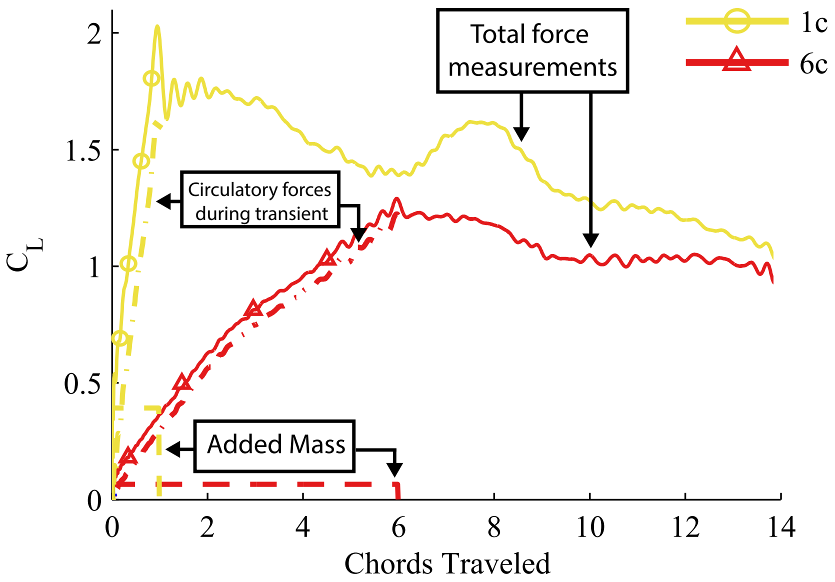

Figure 5: Force histories of the fast ($s_a/c = 1$) and slow ($s_a/c = 6$) cases showing the contributions of circulatory and non-circulatory effects. From Ref. 19.

tight, coherent vortex upon startup, and the vortex remains this way through $s/c = 1.5$. The slow case, however, forms a much weaker leading edge vortex that quickly dissipates as it convects from the wing surface. This observation is shown quantitatively by Figure 8, which gives the normalized total circulation above the wing for both the fast and slow wing kinematics. As expected from the larger vortex with higher vorticity (as seen in Figure 7a-b), the fast case produces consistently higher circulation throughout the motion. This analysis shows that despite having nearly identical LEV trajectories, the fast and slow surging cases produce vortices of different strengths, explaining the large difference in force histories.

4.2 Rectilinear Pitch

Figure 9 shows the leading edge vortex trajectories for all of the AVT-202 rectilinear motions, including rectilinear pitch. The wing is shown in black at a 45 degree angle of incidence. Note that for the pitch cases, the wing is at lower angles of incidence at early times. The leading edge of the wing is located at $(0, 0)$. The x-axis is defined in the direction of the free-stream (i.e., horizontal), and the y-axis is vertical. Both axes are normalized by the wing chord. Note also that the vortex paths shown in Figure 9 *do not* all correspond to the same number of wing chord-lengths traveled. For each case, the first LEV that formed on the wing was tracked from the instant it was identifiable until it could no longer be identified as a vortex. This occurred at different points in the wing motion for the different cases. For the fast and slow surge cases, the LEV persisted until 2.60 and 2.34 chords traveled, respectively. The LEV persisted for longer in the pitch cases, lasting until 3.95 chords traveled in the fast case, and 6.40 chords traveled in the slow case.

For all of the cases examined here, the leading edge vortices travel a similar path when near the leading edge of the wing, but diverge as they move downstream. The vortices that form in the pitch cases move along the wing, while those that form in the surge cases move on a trajectory almost normal to that. The trajectories for the pitch and surge cases are remarkably similar for the

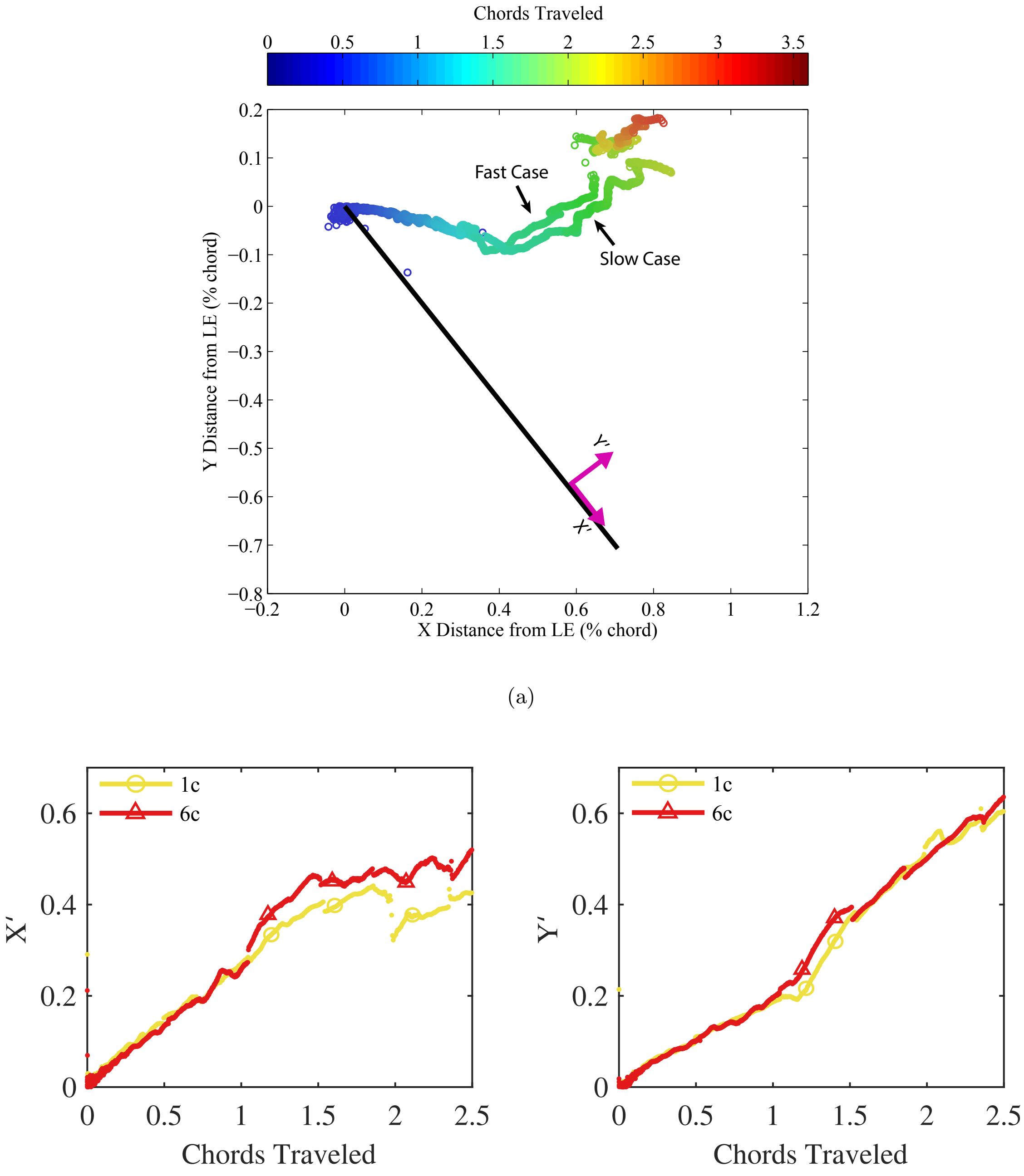

(a)

(b)

(c)

Figure 6: (a) Vortex trajectories in lab-fixed frame for $s_a/c = 1$ (fast) and $s_a/c = 6$ (slow) cases. Trajectories in wing-fixed frame versus distance traveled separated into (b) wing-parallel and (c) wing-normal directions. From Ref. 19.

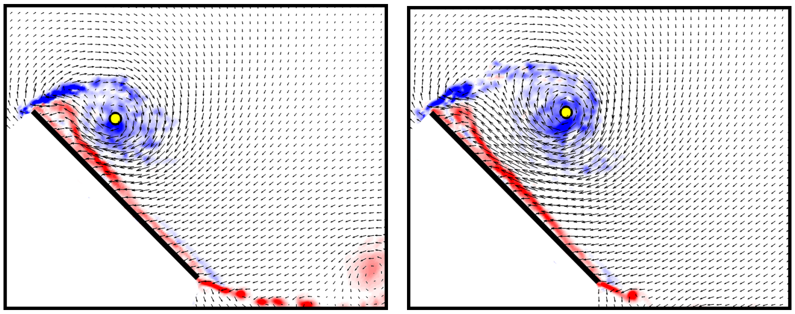

(a) Fast Surge: $s/c = 1$ (b) Fast Surge: $s/c = 1.5$

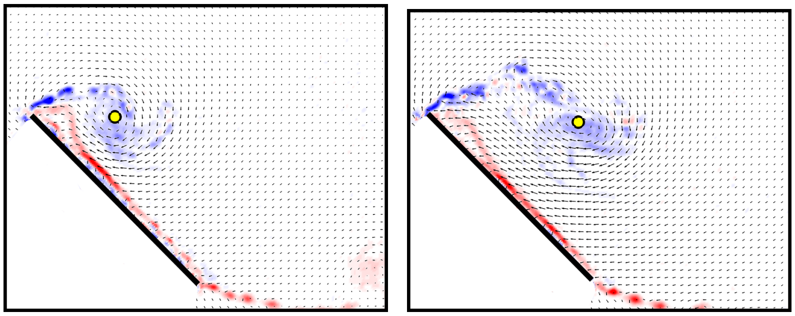

(c) Slow Surge: $s/c = 1$ (d) Slow Surge: $s/c = 1.5$

Figure 7: Contours of vorticity and velocity vector fields illustrating leading edge vortices on fast and slow surging wings. The yellow dot indicates the vortex location as given by the centroid of Γ_1. Only every fifth velocity vector is shown here. From Ref. 19.

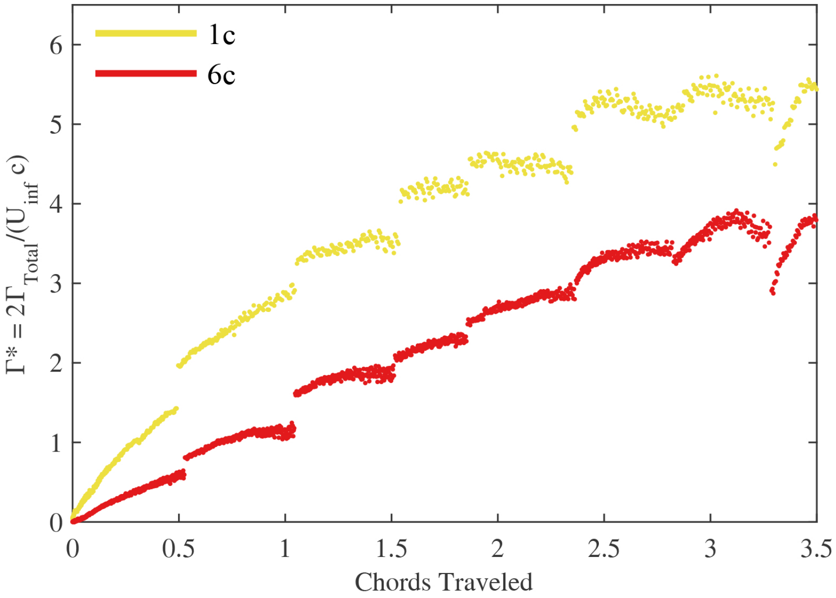

Figure 8: Normalized total circulation for surge cases versus distance traveled. From Ref. 19.

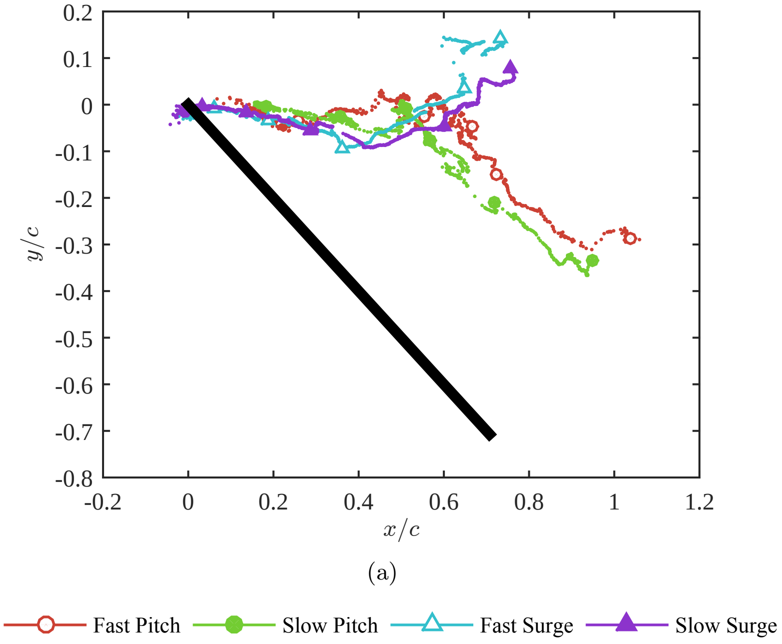

Figure 9: Path of the LEV in the wing-fixed reference frame. From Ref. 18.

fast and slow accelerations, however, suggesting that the path of the vortex is dependent largely on the angle of attack history and not the timescale of the motion.

Figure 10 gives the path of the LEV as a function of convective time. In these plots, the leading edge of the wing is at 0 on the ordinate axis. The x and y positions of the LEV as a function of chords traveled are shown in Figures 10(a) and 10(b), respectively. Figure 10(a) also contains a dashed line with a slope of one, corresponding to the free-stream velocity. At the start of the wing motion, both rectilinear surge cases immediately produce an identifiable vortex at the leading edge. The fast pitch case does not form an LEV until 0.5 chords traveled, and the slow pitch case does not form a vortex until 1.5 chords traveled. It is also clear from Figures 10(a) and 10(b) that the vortices neither leave the wing at free-stream velocity, nor remain attached to the wing.

Plotted in Figure 10 versus chords traveled, the two surge cases still exhibit extremely similar behavior, even for the radically different wing accelerations. The change in direction to almost directly away from the wing, seen in Figure 9, shows up as the change in slope in Figure 10(a) at 1.5 chords traveled. In the y versus s/c graph, Figure 10(b), the largest difference in LEV path is visible: the paths diverge at 2 chords of travel. The two pitch cases are much less alike. In both x and y, these profiles appear to be similar to each other, but stretched along the chords-traveled axis.

As the LEV is fed by a shear layer originating at the leading edge, it was hypothesized that the stretching factor between the pitch cases is related to the rate at which vorticity is generated at the leading edge [18]. As a first step in this direction, a new scaling called σ was computed and is given by

$$\sigma(t) = \int_0^t U(\tau)\sin\left(\alpha(\tau)\right)d\tau \tag{4}$$

where t is the current time and $U(\tau)$ and $\alpha(\tau)$ are the instantaneous velocity and pitch angle, respectively, at time τ. For the surge cases, α is a constant, and thus σ is directly proportional to

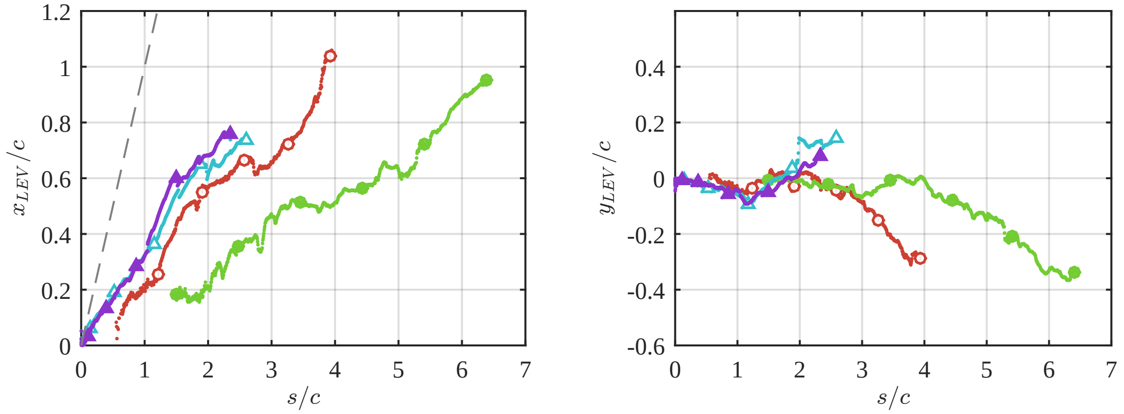

(a) x_{LEV} vs s/c (b) y_{LEV} vs s/c

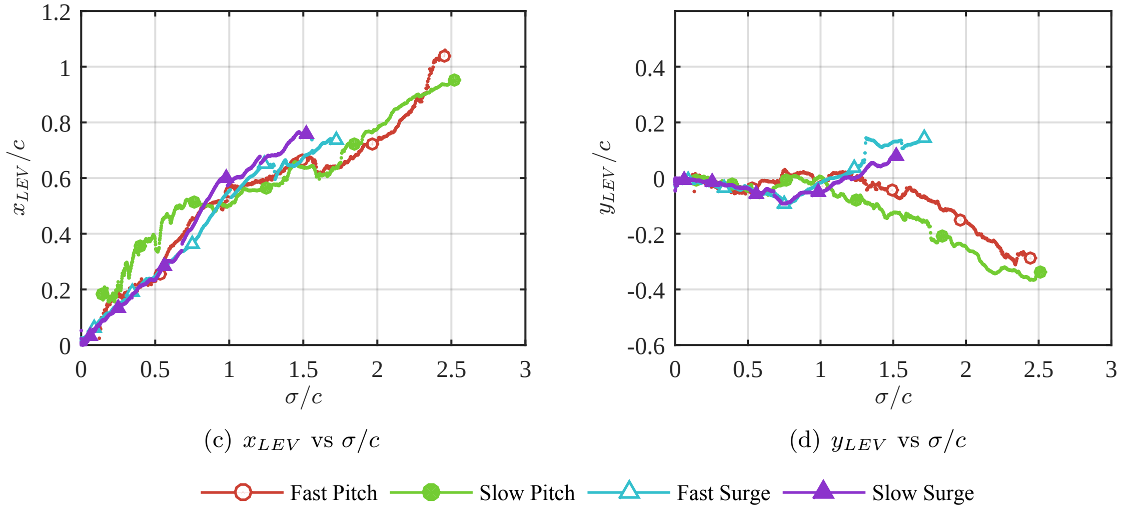

(c) x_{LEV} vs σ/c (d) y_{LEV} vs σ/c

Figure 10: Vortex trajectories over time. Locations are relative to the leading edge of the wing. From Ref. 18.

the distance traveled, s. This is not true for the pitch cases, where α varies as a function of time.

Figures 10(c) and 10(d) show the result of plotting the vortex location measurements with respect to σ, rather than s. The vortex x positions, shown in Figure 10(c), now show a single trend across all cases, including the slow pitch case. The vortex y locations, shown in Figure 10(d), show similar collapse. Of note again is the collapse of the slow and fast pitch data. The difference between the surge and pitch cases still remains, now at $\sigma/c = 1.25$. It is thought that this is due to the effect of the trailing edge vortex as the pitch cases should produce much stronger TEVs than the surge cases.

It is important to note that the leading edge vortex does not move at the free-stream velocity (corresponding to the dashed line in Figure 10(a)), or with the wing (corresponding to a constant x and y values) at any time for the tested kinematics [18]. The vortices are neither fully attached to the wing nor fully detached from the wing. The vortex is slowly left behind as the wing moves away.

The circulation measurements of the leading edge vortex are given in Figure 11. In the current coordinate system, the LEV consists of negative vorticity, hence a more negative value corresponds

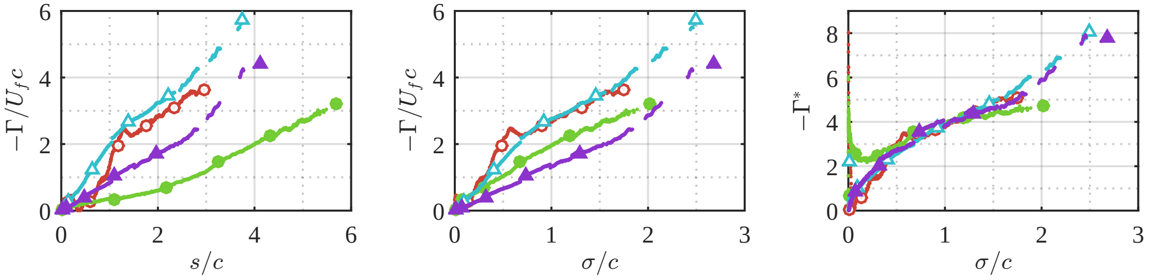

(a) Circulation versus chords traveled (b) Circulation versus leading edge normal chords traveled (c) Instantaneous normalized circulation (Equation (5)) versus leading edge normal chords traveled

Figure 11: Three different normalizations of LEV circulation. From Ref. 18.

to a stronger LEV. Figure 11(a) shows the LEV circulation normalized by the final wing velocity, and plotted against chords traveled, s/c. This produces a wide range of circulation values, to which the same stretching parameter from the locations, σ/c, was applied, producing Figure 11(b). Plotting the data versus σ/c unifies the timing of the circulation growth, but not the magnitudes. The normalization of the circulation measurements was then changed following the same logic as in defining the x axis stretch factor, σ: the instantaneous leading edge-normal velocity was used to normalize the circulation [18]. The resulting quantity has been given the notation Γ^*:

$$\Gamma^* = \frac{\Gamma}{U(t)\sin(\alpha(t))c} \tag{5}$$

where $U(t)$ and $\alpha(t)$ are once again the instantaneous velocity and angle of attack. As Figure 11(c) shows, this gives a good collapse of the circulation measurements, similar in quality to the collapse of LEV location. The collapse of circulation with these two leading edge-normal parameters further substantiates the hypothesis that the vorticity generated at the leading edge is directly related to the leading edge-normal velocity, and that it is the dominant factor in the evolution of the LEV [18].

4.3 Rotational Surge

Rotational motions were the focus of the current work. Experiments focused on the $1c$ fast and $6c$ slow accelerations, and included direct force measurements as well as PIV.

4.3.1 Forces on a Rotating Wing

A sample lift history for the current experiments are given in Figure 12. The lift history shown here corresponds to a single revolution of the wing (i.e., the wing does not encounter its own wake). Deceleration to rest past $\Psi = 360°$ is not shown. During the acceleration of the wing (shaded region, $\Psi \leq 30°$), lift rapidly grows from zero to a local peak coincident with the end of the unsteady wing motion. During this time, non-circulatory effects (i.e., added mass) play a significant role in force generation. Beyond this point, non-circulatory forcing goes to zero, but the measured lift continues to rise until $\Psi = 120°$. From $\Psi = 30°$ to $120°$ lift increases as the flow develops around the wing. Similar lift histories have been measured in many experiments and computations, for example in Refs. [1, 2, 4, 7, 14, 23, 26].

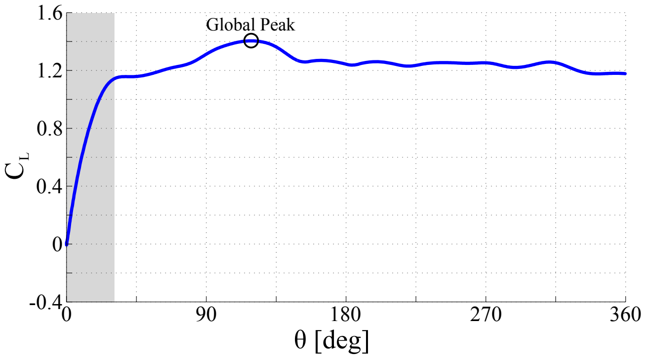

Figure 12: Lift coefficient versus azimuthal angle Ψ for a rotating $\mathcal{R} = 2$ flat plate wing at $Re = 2500$ and $\alpha = 45°$.

4.3.2 Leading Edge Vortex Structure

The three-dimensional structure of the leading edge vortex is most easily seen in dye flow visualization images like those in Figure 13. In the current work, dye flow visualization has been performed over a wide range of azimuthal angles and with a wide variety of dye-injection points. All of the images reveal a LEV that remains attached to the wing and is coherent near the wing root, but bursts near 50% span. These observations are consistent with other work including Refs. 4, 7, 9, 22, 23, 25. Vortex burst is defined here as the sudden expansion of the cross-sectional area of the vortex. At $\Psi = 60°$ and 90°, dye has not convected all the way to the wing tip, but the coherent vortex on the inboard section of the wing is clearly visible. Since the structure of the vortex near the wing root is coherent this vortex is said to be pre-burst. Near the mid-span, a region of accumulated dye is visible, suggesting a change in the axial flow through the vortex core. This phenomenon is characteristic of vortex burst. At $\Psi \geq 120°$, the dye has penetrated the accumulation region and the burst vortex is visible outboard of this point. At $\Psi = 180°$ of rotation, a fully burst leading-edge vortex is visible. The most overt difference in the leading-edge vortex here is the considerable expansion of the structure. Initially confined to the leading edge of the wing (inboard of the midspan), the LEV now encompassed the entire wing surface on the outboard section of the wing, extending from the leading to the trailing edge. Vortex burst affects not only the size, but also the structure of the LEV. Post burst, the previously smooth helical streaklines reveal a large degree of mixing and a less coherent vortical structure. However, despite the loss of coherency, the leading-edge vortex remains attached to the wing surface for the duration of the wing stroke.

4.3.3 Leading Edge Vortex Characteristics

The trajectory of the leading edge vortex on a rotating wing is given in Figure 14 and the corresponding vortex strength is given in Figure 15. In each figure, each curve represents a different spanwise locations. Two runs were conducted at each span location; these runs agreed well and have been ensemble-averaged. The symbols mark the vortex locations at discrete azimuthal positions of 10°, 20°, 30°, 60°, 90°, 180°. Data are only available at discrete angles because the wing was only normal to the laser sheet at those instants. The measurements for the comparable rectilinear wing motions have also been included, and are shown in black. The vortex positions are shown versus σ/c, with σ/c computed locally for each spanwise position on the rotating wing. Note that at each azimuthal angle, the number of chords traveled varies linearly along the wing span, and thus σ/c also varies along the span.

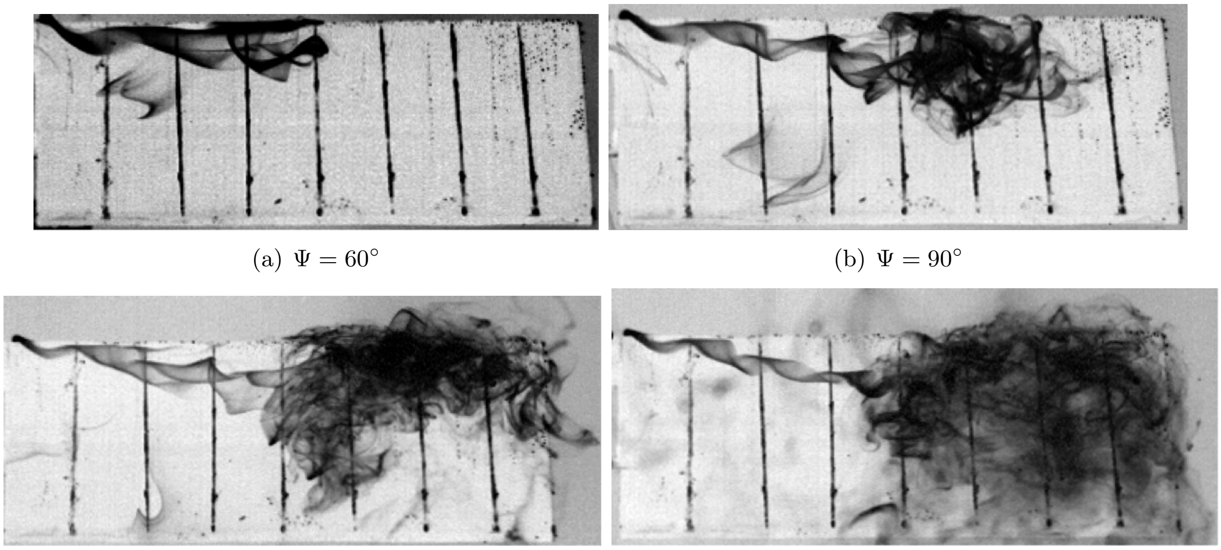

(a) $\Psi = 60°$ (b) $\Psi = 90°$

(c) $\Psi = 120°$ (d) $\Psi = 180°$

Figure 13: Dye flow visualization of the leading edge vortex at $Re = 2000$.

Figure 14 shows the LEV trajectories measured on the rotating wing and compares them to the corresponding data for rectilinear surge. The left column of this figure contains data from the slow (6 chord) acceleration, and the right contains data from the fast (1 chord) acceleration. Figures 14(a) and 14(b) show the path of the LEV through space relative to the wing. Only small deviations are seen here between span locations and it can be seen that path variations in the y-direction are small. Further analysis will thus focus on the LEV x location results as a function σ/c shown in Figures 14(c) and 14(d).

Figures 14(c) and 14(d) show the most obvious difference between the translation and rotating cases—the vortex on the rotating wing remains attached to the wing. This can be seen as the relatively constant value of x_{LEV}/c for the inboard (20%, 30%, and 50% span) sections of the LEV at long time. All of the sections of the LEV in the rotational case follow a very consistent location history (i.e., rate of change of x_{LEV}/c location) until the vortex section settles into its final location, which varies with span location due to the conical shape of the vortex. The time at which a spanwise location becomes constant also depends on the spanwise location itself. Near the wing root, the LEV settles faster and closer to the wing than it does at more outboard locations. Near the wing tip, the vortex does not appear to remain attached at all and becomes unidentifiable, similar to the rectilinear cases.

The attached vortex observed on a rotating wing is in contrast to the detached one that was observed on the wing in rectilinear motion (shown in black in figures 14(c) and 14(d)), where the x position continues to increase until the vortex becomes impossible to track. The vortex trajectories for the rectilinear cases are strikingly similar to those of the rotational cases until $\sigma/c \approx 0.75$. The attachment of the LEV in a rotational motion has serious implications for any force-prediction model that seeks to account for the lift from the leading edge vortex. The mechanism for LEV attachment in the rotating case must be carefully addressed if a successful model is to be created for this flow.

Vortex strength (normalized by the final wing velocity at 75% span) is given in Figures 15(a) and 15(b). The magnitudes of vortex strength are similar for both the rotational and rectilinear kinematics, as is the timescale of formation on the σ/c axis. The circulation histories are also shown

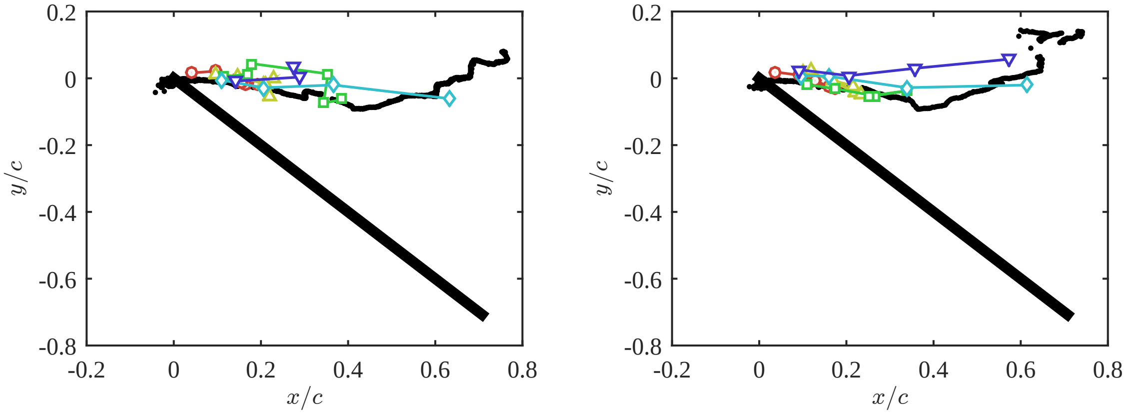

(a) LEV path through space for rotational slow surge (b) LEV path through space for rotational fast surge

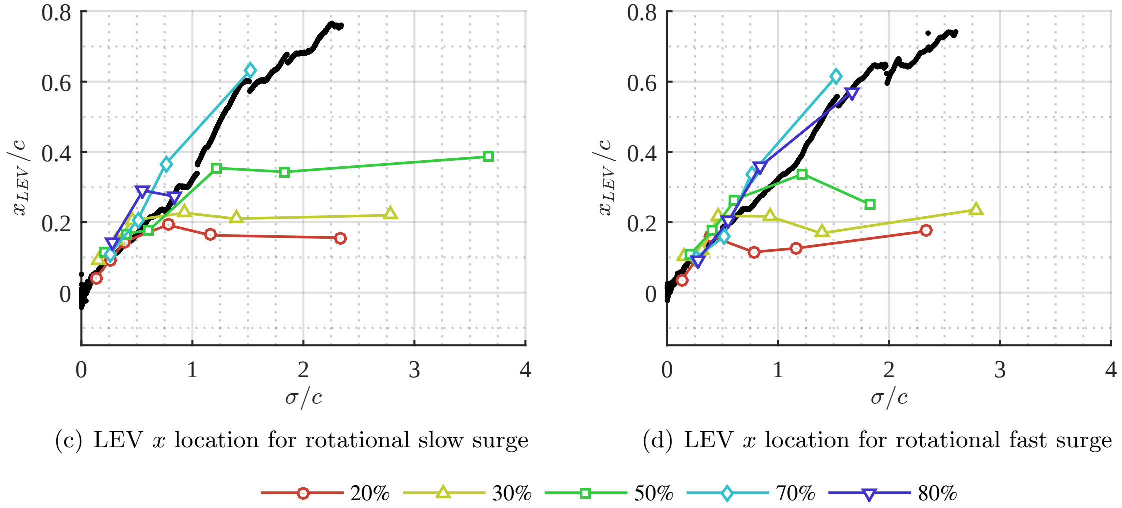

(c) LEV x location for rotational slow surge (d) LEV x location for rotational fast surge

Figure 14: LEV trajectory for rotational slow and fast surge. Rectilinear data for the corresponding case is shown in black. From Ref. 18.

normalized by the local leading edge normal velocity, shown in Figures 15(c) and 15(d) as a function of Γ^*. This normalization collapses the magnitudes of the circulation histories, in particular for the fast case. At small σ/c (< 1) the normalization produces values of rotational Γ^* much greater than those of the rectilinear case. After $\sigma/c = 1$ however, the instantaneous normalization does an excellent job of collapsing the rotational data across the span, as well as with the rectilinear data. This is at odds with the LEV trajectories, which emphasized the differences between the rotational and the rectilinear kinematics as early as $\sigma/c \approx 0.75$. The similarities of the LEV circulation values, Γ^*, between the two types of wing motion suggests that some other flow feature, such as the tip vortex or trailing edge vortex, is responsible for the different vortex trajectories.

4.3.4 The Effect of Tip Clearance on Force Production

Early experiments in this work revealed a local maximum in lift coefficient near 90 degrees of wing rotation (see Fig. 16, for example). Because the wing was started normal to a wall (in the square tank) at $\Psi = 0°$, $\Psi = 90°$ corresponds to the next wall-encounter, and there was concern that this

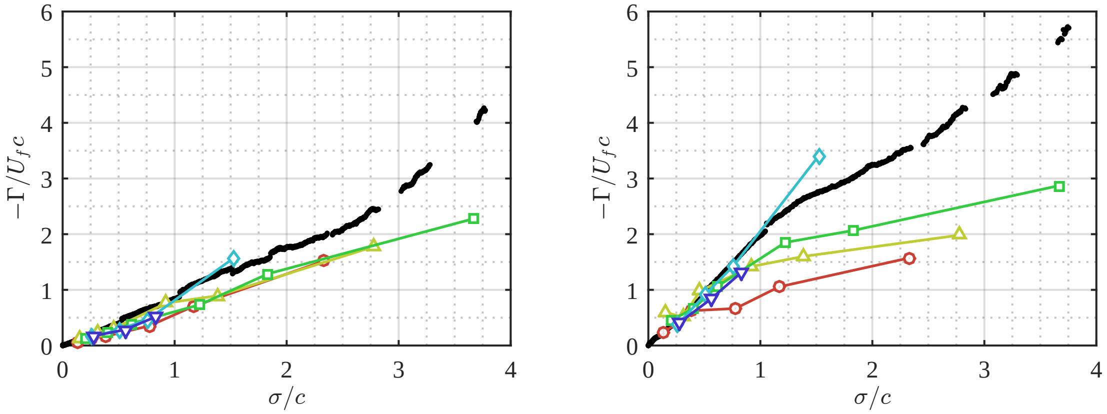

(a) Normalized circulation for rotational slow surge (b) Normalized circulation for rotational fast surge

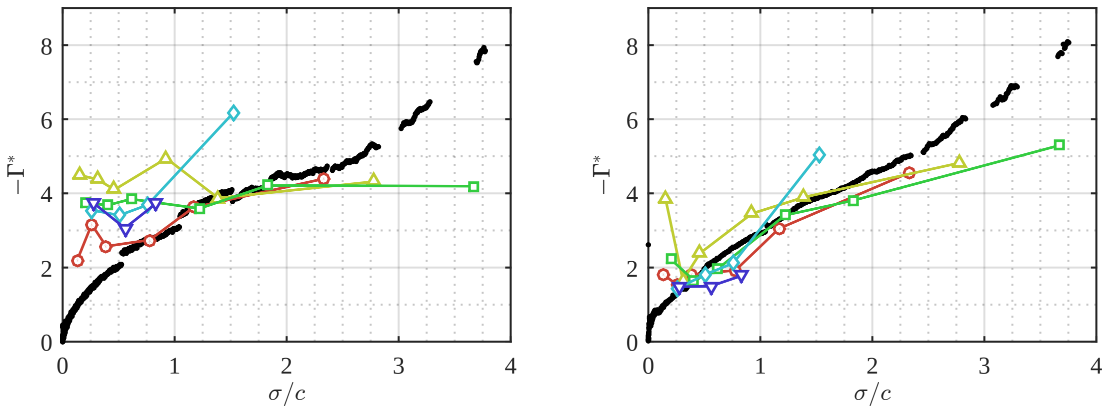

(c) Instantaneous normalized circulation for rotational slow surge (d) Instantaneous normalized circulation for rotational fast surge

Figure 15: LEV circulation over a rotating wing in slow and fast surge. Rectilinear data once again in black. From Ref. 18.

lift peak may be an artifact of the experimental setup. To investigate this possibility, an in-depth study of tip clearance (i.e., the distance from the wing tip to the wall) was undertaken [16].

Figure 16(a) illustrates how C_L varies with tip clearance for a fixed Reynolds number. At $Re = 500$, the $3c$ and $5c$ force curves are a similar shape and lie within 0.1 of each other. If one takes the $5c$ case as sufficiently far from the wall that it has no effect, the proximity of the curves indicates that there are no wall effects in the $3c$ case at $Re = 500$. The $0.5c$ data, however, is significantly different. The upward shift is indicative of a suppression of the tip vortex due to wall interaction. At $Re = 2500$, the data for $0.5c$, $3c$, and $5c$ is shifted up with respect to the $Re = 500$ case. Because this occurs for all tip clearances, even the very large ones, the data indicate that this is likely not a tip clearance effect, but a Reynolds number effect (see Figure 17). The different tip clearances are no longer as clearly grouped as at $Re = 500$. The $0.5c$ data has garnered a very sharp peak at $\Psi = 540^\circ$, but it is worth noting that the $3c$ and $5c$ cases do not have a peak at $\Psi = 540^\circ$, pointing to a significant reduction in wall effects between $0.5c$ clearance and $3c$ clearance. At $Re = 10000$, the $0.5c$ and $3c$ cases are similar and at a higher C_L than the $5c$ case. This suggests

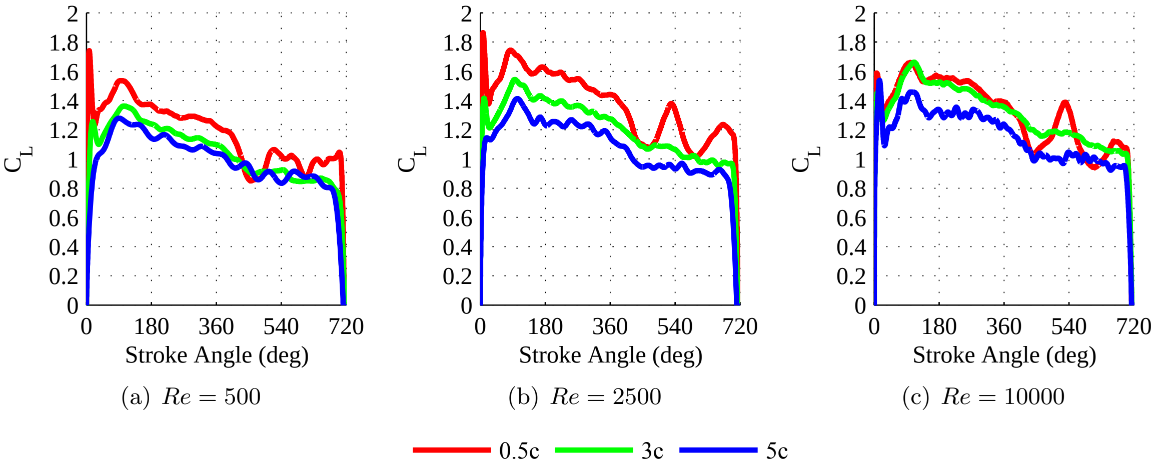

(a) $Re = 500$ (b) $Re = 2500$ (c) $Re = 10000$

Figure 16: Comparison of lift coefficients at constant Reynolds number, from Ref. 16.

that the $3c$ case is impacted by the wall at this higher Reynolds number. Due to experimental limitations, it was not possible to acquire force measurements for larger tip clearances, but CFD, flow visualization and PIV suggest that the $5c$ case is not affected by the walls, nor is a $7c$ case [16].

The tip clearance study summarized above lead into a study of the effect of Reynolds number on the force coefficients. The lift histories for each of the test cases are organized by tip clearance and presented in Figure 17. In general, it appears that C_L increases slightly with Reynolds number. Figure 17(a) shows the lift histories acquired with $0.5c$ tip clearance for all Reynolds numbers. The C_L curve for $Re = 500$ is almost 0.2 higher than the $Re = 120$ case. Reynolds numbers greater than 500 resulted in even larger forces, but cluster within error into a single force curve. This suggests that above $Re = 2500$ the lift coefficient is independent of Reynolds number (for this tip clearance). A large peak at $\Psi = 540°$ also appears to be a consistent trend for Reynolds number of 2500 and greater. Because this peak corresponds almost exactly with passage near a wall, tests were also conducted starting the wing at $\Psi_0 = 45°$, aligned with the corner rather than the wall of the tank, delaying this wall passage by 45° to 495° of rotation. The large force peak shifted by almost exactly 45° to $\Psi = 495°$, confirming that it is related to the point at which the wing tip passes the wall most closely. It is interesting, however, that this peak does not exist in the first revolution (i.e., at $\Psi = 540 - 360 = 180°$), nor at any other wall passage (i.e., $\Psi = n90°$). The smaller force peak that appears at $\Psi = 90°$ did not move when the wing was started at the new location, but was fixed at the point where the wing passes through 90° of rotation.

Figure 17(b) shows the lift histories for a wing with $3c$ of tip clearance. Notably absent from all of these cases is the peak at $\Psi = 540°$ that was previously seen for the $0.5c$ cases. Data for the $3c$ clearance at $Re = 500$, 1000, and 2500 show an increasing trend with Reynolds number. Like the $0.5c$ case, the higher Reynolds numbers lie on top of each other, but it should be noted that the Reynolds number at which the force curves begin to match, $Re = 7500$ and 10000, is higher for the case with greater tip clearance. Figure 17(c) shows the lift histories for the wing with $5c$ of tip clearance. Here, only the $Re = 120$ clearly lies below the others.

The effects of Reynolds number and tip clearance on the magnitude of the lift coefficients are summarized in Figure 18. Here, each marker represents an average of the unsteady lift coefficient as measured between $\Psi = 180°$ and $\Psi = 270°$, the portion of the first revolution where the forces are nearly constant. These time-averaged lift coefficients give a good indication of the overall

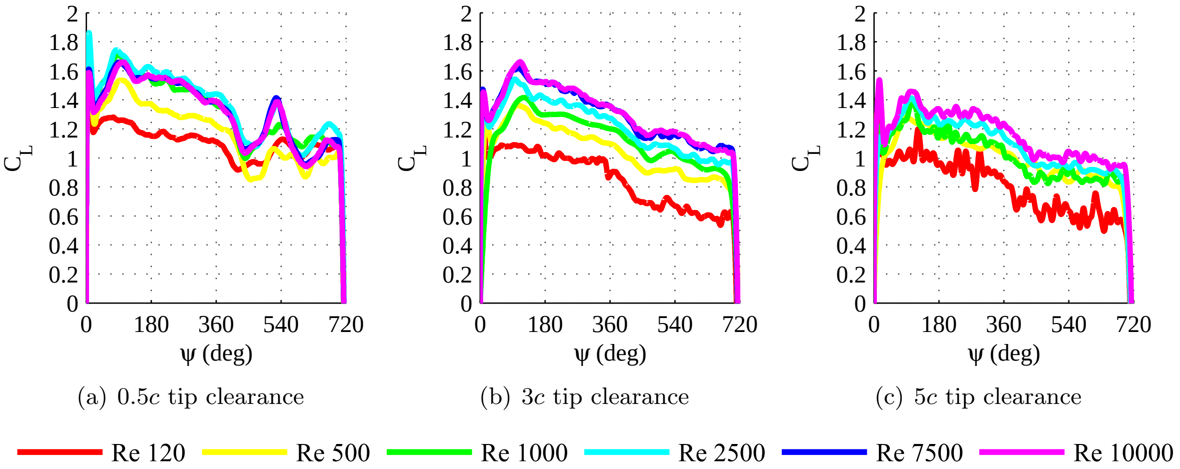

(a) 0.5c tip clearance (b) 3c tip clearance (c) 5c tip clearance

Figure 17: Comparison of lift coefficients at constant tip clearance, from Ref. 16.

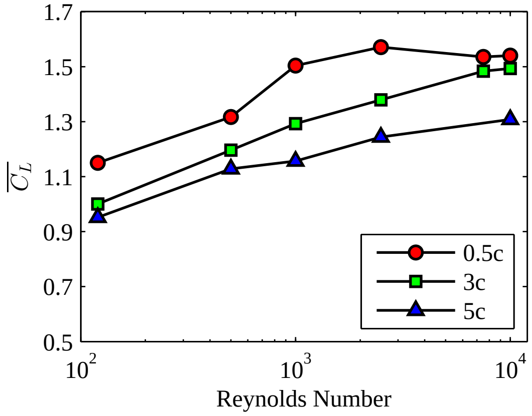

Figure 18: Average lift coefficient over $180° \le \Psi \le 270°$ versus Reynolds number for the three tip clearance cases. From Ref. 16

magnitude of forces recorded for each case, and highlight the trends across both Reynolds number and tip clearance. All of the Reynolds numbers show an increasing trend in $\overline{C_L}$ with decreasing tip clearance, though some lie very near each other. Starting on the left side of the plot at $Re = 120$ and $Re = 500$, the 3c and 5c values are similar. If the 5c case is considered to be far from the wall, their proximity indicates that there are no wall effects occurring for the 3c case at these low Reynolds numbers. The 0.5c data is displaced upwards significantly, and significant wall effects are expected to be visible in the flow field. As Reynolds number increases, the 3c and 5c data separate as wall effects begin to creep into the 3c data. The averaged lift coefficient for the 3c case continues to increase for Reynolds numbers as high as 7500, while the 0.5c values level out, and at higher Reynolds numbers, the 3c case results in a lift coefficient almost as high as the 0.5c tip clearance case. Comparing the $Re = 120$ data points in Figure 18 with those at $Re = 10000$, it appears that when designing an experiment to avoid wall effects, a smaller tip clearance may be acceptable at lower Reynolds numbers than at higher ones.

4.3.5 Characteristics of the Trailed Tip Vortex

A related study is that of the tip vortex structure, time scale of formation, and effect of wall proximity [16]. Figure 19 shows the evolution of the tip vortex at $Re = 10000$ near the start of the wing motion for the three tip clearance cases. The tank walls are shown as solid black lines, the axis of rotation as a dashed line, and the wing (when it is in the field of view) as black if in front of the laser sheet and grey if behind it. The color contours represent the vorticity field, normalized by the wing chord and velocity at R_{75}. Solid black contours indicate coherent vortex structures satisfying $|\Gamma_2| > 2/\pi$ [8]. The yellow bullets (●) indicate the vortex center, and the position of the vortex center is given by r_x and r_y. The tip vortex that appears in these images was shed at the start of the wing motion, $\Psi = 0°$, and is shown at various wing stroke angles spanning $\Psi = [60°, 120°, 180°]$, ordered by column in ascending order of wing tip clearance. Operating with a tip clearance of $0.5c$ causes the tip vortex to form very near the wall, resulting in behavior markedly different from greater clearances. The vorticity distribution of the $0.5c$ case includes a system of vortices, visible as multiple peaks in the vorticity field (see $0.5c$ at $\Psi = 60°$). In time, the dominant vorticity peak induces a clockwise motion of the secondary peak. Come stroke angle $\Psi = 180°$, there exists significant clockwise rotation on what remains of the tip vortex which now appears much smaller and weaker.

In contrast, the $3.0c$ tip clearance wing generates a tip vortex that largely maintains a circular shape, seemingly unimpeded by the wall boundary. The vorticity distribution is localized to a single peak, instead of spreading out as for the $0.5c$ case. Further enlargement of tip clearance to $5.0c$ also produces a circular tip vortex. However, given the relatively small wing span and large wing mounting strut, the tip vortex is introduced into the flow near the wake of the wing mount and force balance, which acts to perturb the vortex shape. To better determine the potential for the tip vortex initiated at $\Psi = 0°$ to alter the wake for subsequent revolutions, and therefore force generation, the circulation of the identified vortices are quantified.

Figure 20 shows the circulation strength of the tip vortex as defined by the Γ_2 criterion. It is important to note that the circulation values presented here correspond to the tip vortex initiated at $\phi = 0$, with evolution measurements confined to a fixed plane (i.e., the plane illuminated by the laser sheet). Circulation strengths presented here begin for stroke angle 35°, when the wing no longer obstructs tip vortex visibility. Of the clearances tested, the $3.0c$ case produced the greatest nondimensional circulation, obtaining a maximum early in the stroke, before strength begins to decline at approximately $\Psi = 110°$. The $5.0c$ case demonstrates an early peak, followed by relatively steady strength for the remainder of the range. When the tip clearance is reduced to $0.5c$, the corresponding tip vortex strength attains a maximum near inception, then steadily diminishes in strength to negligible values before the wing reaches $\Psi = 180°$, as alluded to earlier in the discussion of Figure 19.

4.3.6 Effect of Wall Boundaries on the Tip Vortex at the Wing

The effect of the proximity of the tank walls is not limited to wake dissipation, but perhaps more importantly impacts the attached, tip vortex. To demonstrate the tip vortex response, Figure **??** shows the effects of tip clearance on the flow field at wing stroke position $\Psi = 180°$. Beginning with the greatest tip clearance of $5.0c$, it is found that the area of the active tip vortex, A_{TV}, measures 19% of the wing planform area, S, where vortex area here is determined as the area in-plane satisfying the Γ_2 criterion. Furthermore, the tip vortex extends inboard the wing tip a distance of 34% of the wing span as measured by the distance from the wing tip to the furthest inboard point on the Γ_2 contour. The tip vortex on the $3.0c$ clearance wing behaves similarly, with

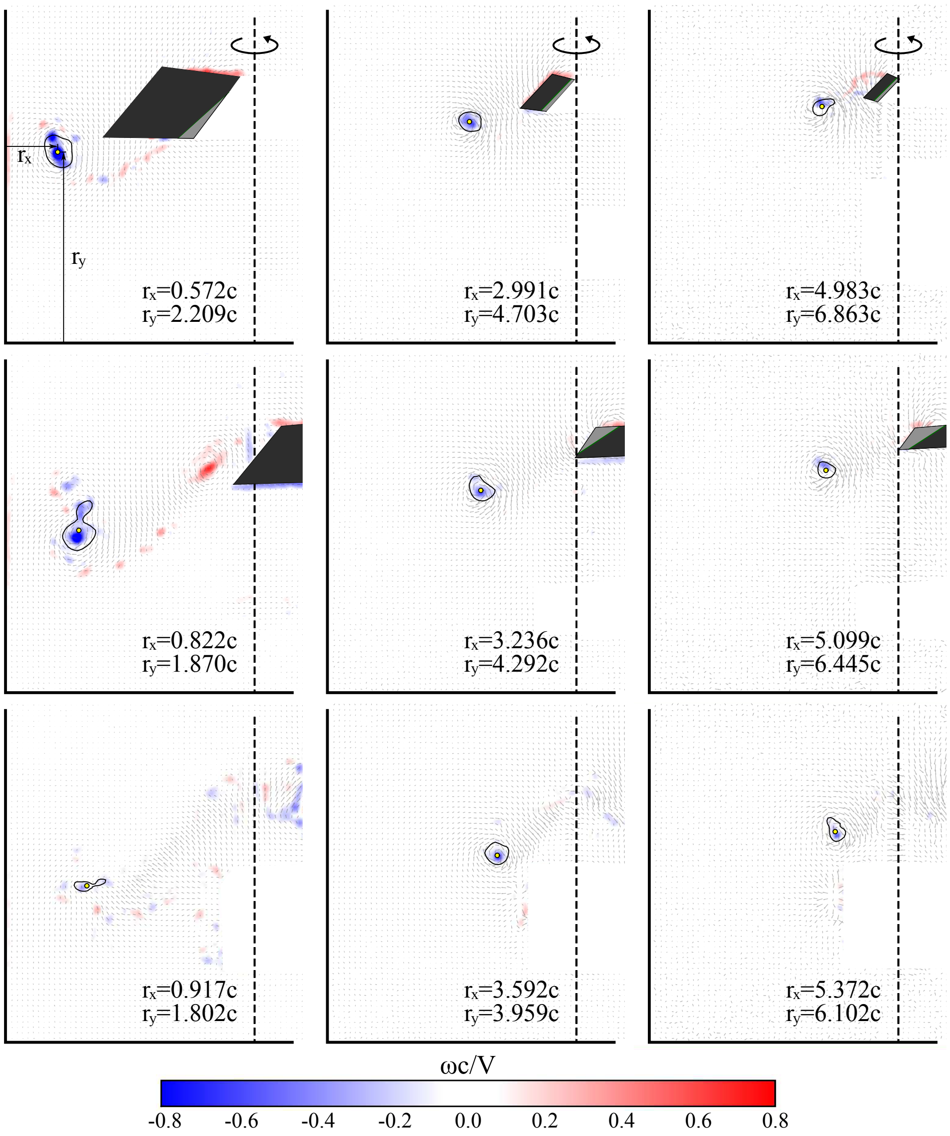

Figure 19: Tip vortex development during wing rotation. Rows: $\Psi = [60°, 120°, 180°]$. Columns: Tip clearance $5.0c$ (left), $3.0c$ (center), and $0.5c$ (right). From Ref. 16.

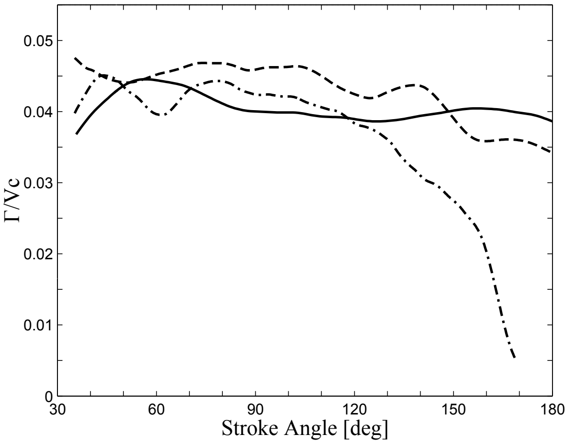

Figure 20: Tip vortex strength for wake age $0^\circ \leq \Psi \leq 180^\circ$ of a vortex initially introduced at $\Psi = 0^\circ$ and $Re = 10000$. Tip clearance: $5.0c$ (—), $3.0c$ (− − −), $0.5c$ (− · −). From Ref. 16.

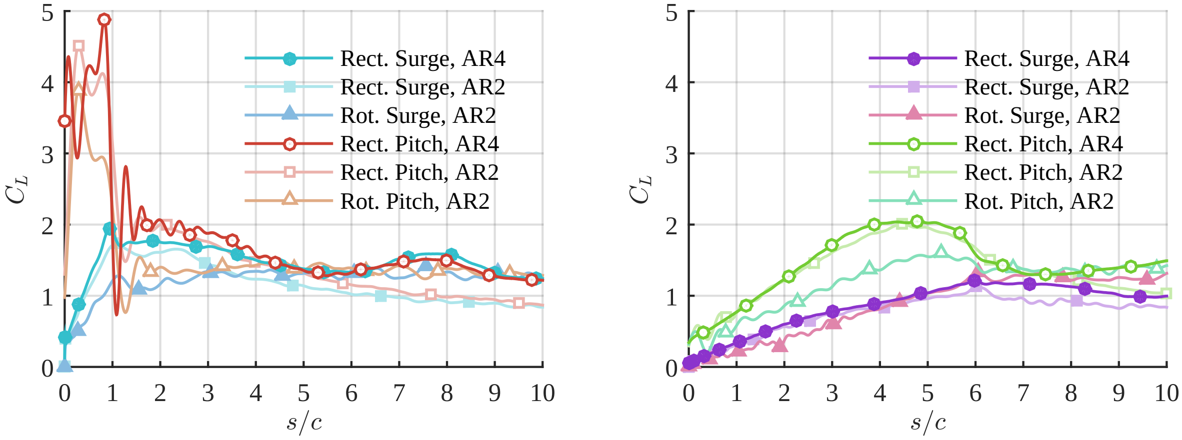

(a) The fast ($1c$) cases

(b) The slow ($6c$) cases

Figure 21: Lift coefficient histories grouped by acceleration. From Ref. 18.

an area measuring 18% of the wing planform area and extending inboard 32% span. It is also worth noting that the tip vortices for the $5.0c$ and $3.0c$ tip clearance cases are well defined, a stark contrast to that of the $0.5c$ case.

Closing the tip clearance to $0.5c$ alters not only the size of the vortex, but also the vorticity field. The proximity of the tank wall acts to shift the tip vortex further inboard on the wing, now extending 58% span from the wing tip to the furthest Γ_2 contour point detected (see Figure **??** (right)). In this case, the area associated with the tip vortex appears to undergo mixing that is absent in the larger tip clearances.

4.4 Comparison of the AVT-202 Test Cases

A comparison of the complete set of the AVT-202 test cases is given in the form of force histories grouped by wing acceleration in Figure 22 and type of motion in Figure 22. Only the first ten chords of travel are presented here, corresponding to the extent of the vortex data shown previously.

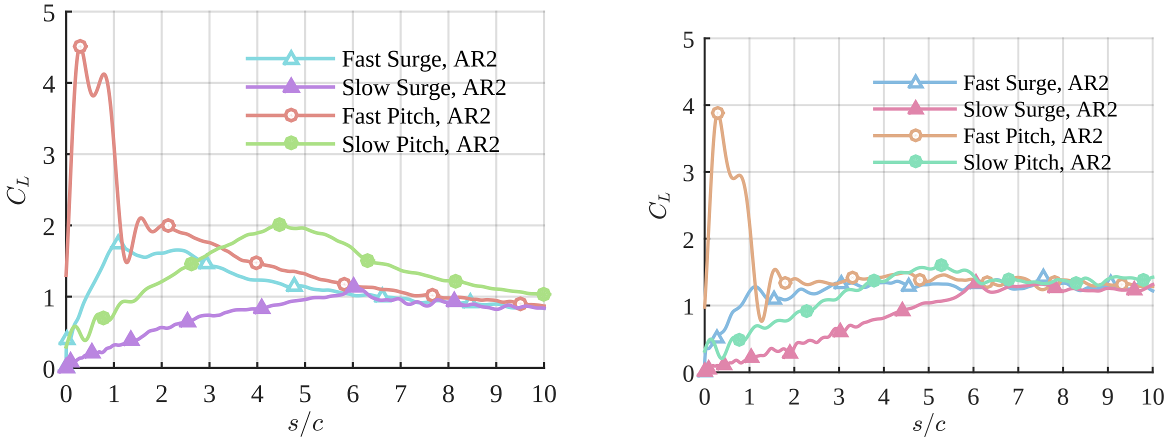

(a) The rectilinear cases

(b) The rotation cases

Figure 22: Lift coefficient histories grouped by type of motion. From Ref. 18.

Figure 21 shows the lift histories for the 1 and 6 chord acceleration cases, rectilinear and rotational pitch and surge. Note that two different aspect ratios are represented in the data: an aspect ratio 2 wing, and an aspect ratio 4 wing. All of the curves shows an increase in lift during wing acceleration, followed by a relatively benign settling to steady state well after the end of acceleration. For the pitch cases, there is a large transient near the start of the wing motion. The surge cases do not exhibit the same extreme transient behavior. The shape of the force history during wing acceleration is related to whether the wing is moving in pitch or surge than than whether it is a rectilinear or rotational motion. After the wing reaches a constant speed and/or incidence angle, the force histories for all motions tested converge and begin approaching a steady state [18].

The differences in the force histories of the rectilinear and rotational cases are relatively small. The pitching wing in rotation exhibits less force during the pitching motion and more force in steady state than do the wings in rectilinear motions, but the magnitude of the differences is smaller than might be expected for two fundamentally different sets of kinematics. In steady state, the higher lift coefficients observed on the rotating wing may be attributed to the presence of an attached LEV, the choice of a reference velocity in the nondimensionalization [26], or a combination of the two. The differences in forces on an aspect ratio 2 or 4 wing undergoing rectilinear motion are also slight. The primary discrepancy in the fast case is the slight rise in the aspect ratio 4 data at 7.5 chords of travel, which is believed to be associated with a vortex shedding and reformation event [19].

Figure 22 shows the aspect ratio 2 force data to highlight differences due to the magnitude of wing acceleration. The magnitude of non-circulatory lift produced during the pitching motion is much smaller for the wing that accelerates more slowly. (I.e., the maximum lift measured in the fast rectilinear and rotational pitch cases is larger than that measured in the slow rectilinear and rotational pitch cases.) For both rotational and rectilinear motions, the force histories are insensitive to the wing's initial acceleration once the wing has reached a constant velocity. The force histories of the rectilinear motions exhibit a much longer settling time to steady state than do those of the rotational motions. The rotational cases reach steady state almost immediately after the conclusion of the unsteady portion of the motion, while the rectilinear cases have been shown to take upwards of 20 chord-lengths of travel to reach steady state [19]. This is likely due to the presence of an attached leading edge vortex in the rotational cases and a shedding vortex in the rectilinear cases. An attached vortex would lead to a relatively stable flow field above the rotating wing, and hence steadier forces than in the rectilinear cases, where vortices continue to form and shed, even in a steady flow [19].

5 Conclusions

By investigating both pitching and surging wings in rectilinear and rotational motion, it was found that the presence of unsteady pitching motions had a greater impact on the lift transients than did the three-dimensionality of the rotational motions, though the structure of the flow was significantly different on the surging wings in rectilinear and rotational motion. The leading edge vortex remained attached to the rotating wing, but was quickly shed from those in rectilinear translation. Furthermore, differences in the force histories between the fast and slow accelerations cannot be explained by added mass or inertial effects alone. Analysis of the flow fields has shown that the strength and trajectory of the leading edge vortex varies with wing acceleration, and relating these trajectories to the force histories suggests that the characteristics of the vortex play a significant role in force production. Leading edge vortex strength and trajectory were found to affect lift even when the vortex was not attached to the wing. Trends in vortex strength and position were found when the parameters were scaled by the velocity normal to the leading edge of the wing.

References

[1] Extensions of Fundamental Flow Physics to Practical MAV Aerodynamics. Technical Report TR-AVT-202, NATO RTO, Sept. 2014.

[2] N. Beals and A. R. Jones. Lift Production by a Passively Flexible Rotating Wing. *AIAA Journal*, 53(10):2995–3005, Oct. 2015.

[3] J. Birch and M. Dickinson. Spanwise flow and the attachment of the leading-edge vortex on insect wings. *Nature*, 412(6848):729–733, Aug. 2001.

[4] Z. R. Carr, A. C. DeVoria, and M. Ringuette. Aspect-Ratio Effects on Rotating Wings: Circulation and Forces. *Journal of Fluid Mechanics*, 767:497–525, Feb. 2015.

[5] A. C. DeVoria and M. Ringuette. Vortex formation and saturation for low-aspect-ratio rotating flat-plate fins. *Experiments in Fluids*, 52(2):441–462, Nov. 2011.

[6] C. P. Ellington. The Aerodynamics of Hovering Insect Flight. IV. Aeorodynamic Mechanisms. *Philosophical Transactions of the Royal Society B: Biological Sciences*, 305(1122):79–113, Feb. 1984.

[7] D. J. Garmann, M. R. Visbal, and P. D. Orkwis. Three-Dimensional Flow Structure and Aerodynamic Loading on a Revolving Wing. *Physics of Fluids*, 25, 2013.

[8] L. Graftieaux, M. Michard, and N. Grosjean. Combining PIV, POD and Vortex Identification Algorithms for the Study of Unsteady Turbulent Swirling Flows. *Measurement Science and Technology*, 12(9):1422–1429, 2001.

[9] R. R. Harbig, J. Sheridan, and M. C. Thompson. Reynolds number and aspect ratio effects on the leading-edge vortex for rotating insect wing planforms. *Journal of Fluid Mechanics*, 717: 166–192, Feb. 2013.

[10] A. R. Jones and H. Babinsky. Unsteady Lift Generation on Rotating Wings at Low Reynolds Numbers. *Journal of Aircraft*, 47(3):1013–1021, May 2010.

[11] A. R. Jones and H. Babinsky. Reynolds number effects on leading edge vortex development on a waving wing. *Experiments in Fluids*, 51(1):197–210, Jan. 2011.

[12] A. R. Jones, F. Manar, N. Phillips, T. Nakata, R. Bomphrey, M. Ringuette, M. Percin, B. van Oudheusden, and J. Palmer. Leading edge vortex evolution and lift production on rotating wings (invited). In *54th AIAA Aerospace Sciences Meeting and Exhibit*, San Diego, CA, 3 2016.

[13] D. Kim and M. Gharib. Experimental study of three-dimensional vortex structures in translating and rotating plates. *Experiments in Fluids*, 49(1):329–339, Apr. 2010.

[14] S. Kolluru Venkata and A. R. Jones. Leading-Edge Vortex Structure over Multiple Revolutions of a Rotating Wing. *Journal of Aircraft*, 50(4):1312–1316, July 2013.

[15] D. Lentink and M. Dickinson. Rotational Accelerations Stabilize Leading Edge Vortices on Revolving Fly Wings. *Journal Of Experimental Biology*, 212(16):2705–2719, July 2009.

[16] F. H. Manar, A. Medina, and A. R. Jones. Tip vortex structure and aerodynamic loading on rotating wings in confined spaces. *Experiments in Fluids*, 55(9):1–18, Sept. 2014.

[17] F. H. Manar, P. Mancini, and A. R. Jones. Vortex Characterization and Force Production on Two- and Three-Dimensional Wing Kinematics. In *AIAA Aerospace Sciences Meeting*, Kissimmee, FL, Jan. 2015. American Institute of Aeronautics and Astronautics.

[18] F. H. Manar, P. Mancini, D. Mayo, and A. R. Jones. Comparison of Rotating and Translating Wings: Force Production and Vortex Characteristics. *AIAA Journal*, pages 1–12, Nov. 2015.

[19] P. Mancini, F. H. Manar, K. Granlund, M. V. Ol, and A. R. Jones. Unsteady Aerodynamic Characteristics of a Translating Rigid Wing at Low Reynolds Number. *Physics of Fluids*, 27 (12):123102, Dec. 2015.

[20] P. Mancini, F. H. Manar, and A. R. Jones. A Semi-Empirical Approach to Modeling Lift Production. In *53rd AIAA Aerospace Sciences Meeting*, Kissimmee, FL, Jan. 2015. American Institute of Aeronautics and Astronautics.

[21] D. B. Mayo and A. R. Jones. Evolution and Breakdown of a Leading Edge Vortex on a Rotating Wing. In *51st AIAA Aerospace Sciences Meeting and Exhibit*, Grapevine, TX, Jan. 2013.

[22] C. A. Ozen and D. Rockwell. Three-dimensional vortex structure on a rotating wing. *Journal of Fluid Mechanics*, 707:541–550, 2012.

[23] M. Percin and B. W. van Oudheusden. Three-Dimensional Flow Structures and Unsteady Forces on Pitching and Surging Revolving Flat Plates. *Experiments in Fluids*, 56, 2015.

[24] C. Pitt Ford and H. Babinsky. Lift and the Leading-Edge Vortex. *Journal of Fluid Mechanics*, 720:280–313, Feb. 2013.

[25] M. Ringuette and A. C. DeVoria. Vortex Formation and Saturation for Low-Aspect-Ratio Rotating Flat-Plate Fins. *Experiments in Fluids.*

[26] K. L. Schlueter, A. R. Jones, K. Granlund, and M. Ol. Effect of Root Cutout on Force Coefficients of Rotating Wings. *AIAA Journal*, pages 1322–1325, 2014.

[27] M. J. Tarascio, M. Ramasamy, I. Chopra, and J. G. Leishman. Flow Visualization of Micro Air Vehicle Scaled Insect-Based Flapping Wings. *Journal of Aircraft*, 42(2):385–390, Mar. 2005.

[28] J. R. Usherwood and C. P. Ellington. The aerodynamics of revolving wings I. Model hawkmoth wings. *Journal Of Experimental Biology*, 205(11):1547–1564, June 2002.

1.

1. Report Type

Final Report

Primary Contact E-mail
Contact email if there is a problem with the report.

arjones@umd.edu

Primary Contact Phone Number
Contact phone number if there is a problem with the report

301-405-7988

Organization / Institution name

University of Maryland

Grant/Contract Title
The full title of the funded effort.

Lift Production on Flapping and Rotary Wings at Low Reynolds Numbers (YIP)

Grant/Contract Number
AFOSR assigned control number. It must begin with "FA9550" or "F49620" or "FA2386".

FA9550-12-1-0251

Principal Investigator Name
The full name of the principal investigator on the grant or contract.

Anya Rachel Jones

Program Manager
The AFOSR Program Manager currently assigned to the award

Ivett Leyva

Reporting Period Start Date

05/15/2012

Reporting Period End Date

11/14/2015

Abstract

The objective of this research was to identify the mechanisms of lift production on models of an entomological flapping wing stroke by evaluating the relative importance of the leading edge vortex, other coherent vortical structures in the flow, bound circulation, and non-circulatory forcing. The entomological wing stroke was modeled as a combination of wing pitch and rotation. In collaboration with the NATO AVT-202 task group on ``Extensions of Fundamental Flow Physics to Practical MAV Aerodynamics", the rectilinear analogs of these rotational motions were also studied. To identify lift-generating mechanisms and relate flow structures to the unsteady forces generated by the wing, synchronized flow visualization, force measurements, and particle image velocimetry (PIV) were recorded for a variety of wing kinematics over a large parameter space. It was found that although the three-dimensionality of the rotational motions resulted in an attached leading edge vortex whereas the leading edge vortex was shed from a wing in rectilinear translation. Wing loading on the rotating wing was such that the resulting lift coefficients were, however, similar. The introduction of an unsteady pitching moment had a greater impact on the lift transient. By comparing both pitching and surging wings in rectilinear and rotational motion over a range of accelerations, it was found that the strength and trajectory of the leading edge vortex had a significant impact on the lift production of a wing undergoing highly unsteady kinematics. The vortex need not be attached to the wing to affect a lift force, and trends in vortex characteristics were found when scaled by the

velocity normal to the leading edge of the wing.

Distribution Statement

This is block 12 on the SF298 form.

Distribution A - Approved for Public Release

Explanation for Distribution Statement

If this is not approved for public release, please provide a short explanation. E.g., contains proprietary information.

SF298 Form

Please attach your SF298 form. A blank SF298 can be found here. Please do not password protect or secure the PDF
The maximum file size for an SF298 is 50MB.

AFD-070820-035.pdf

Upload the Report Document. File must be a PDF. Please do not password protect or secure the PDF . The maximum file size for the Report Document is 50MB.

report.pdf

Upload a Report Document, if any. The maximum file size for the Report Document is 50MB.

Archival Publications (published) during reporting period:

Mancini, P., Manar, F., Granlund, K., Ol, M., and Jones, A. R. (2015). Unsteady Aerodynamic Characteristics of a Translating Rigid Wing at Low Reynolds Number. Physics of Fluids, 27(2). doi: 10.1063/1.4936396

Manar, F., Mancini, P., Mayo, D. B., and Jones, A. R. (2015). A Comparison of Rotating and Translating Wings: Force Production and Vortex Characteristics. AIAA Journal, 2015, accessed December 1, 2015. doi: http://arc.aiaa.org/doi/abs/10.2514/1.J054422

Beals, N., and Jones, A. R. (2015). Lift Production on a Passively Flexible Rotating Wing. AIAA Journal, 53(10), pp. 2995-3005.

Manar, F., Medina, A., and Jones, A. R. (2014). Tip Vortex Structure and Aerodynamic Loading on Rotating Wings in Confined Spaces. Experiments in Fluids, 55(9), pp. 1-18.

Schlueter, K., Jones, A. R., Granlund, K., and Ol, M. (2014). Effect of Root Cutout on the Lift Produced by a Rotating Wing. AIAA Journal, 52(6), pp. 1322-1325.

Kolluru Venkata, S. and Jones, A. R. (2013). Leading Edge Vortex Structure over Multiple Revolutions of a Rotating Wing. AIAA Journal, 50(4), pp. 1312-1316.

Changes in research objectives (if any):

Change in AFOSR Program Manager, if any:

Formerly managed by Doug Smith

Extensions granted or milestones slipped, if any:

NCE granted from May to November 2015

AFOSR LRIR Number

LRIR Title

Reporting Period

Laboratory Task Manager

Program Officer

Research Objectives

Technical Summary

Funding Summary by Cost Category (by FY, $K)

	Starting FY	FY+1	FY+2
Salary			
Equipment/Facilities			
Supplies			
Total			

Report Document

Report Document - Text Analysis

Report Document - Text Analysis

Appendix Documents

2. Thank You

E-mail user

Feb 12, 2016 21:16:17 Success: Email Sent to: arjones@umd.edu